



**HAL**  
open science

# Strength measurement and rupture mechanisms of a micron thick nanocrystalline MoS<sub>2</sub> coating using AFM based micro-bending tests

Guillaume Colas, Peter Serles, Aurélien Saulot, Tobin Filleter

## ► To cite this version:

Guillaume Colas, Peter Serles, Aurélien Saulot, Tobin Filleter. Strength measurement and rupture mechanisms of a micron thick nanocrystalline MoS<sub>2</sub> coating using AFM based micro-bending tests. Journal of the Mechanics and Physics of Solids, 2019, 128, pp.151 - 161. hal-02160926

**HAL Id: hal-02160926**

**<https://hal.science/hal-02160926>**

Submitted on 20 Jun 2019

**HAL** is a multi-disciplinary open access archive for the deposit and dissemination of scientific research documents, whether they are published or not. The documents may come from teaching and research institutions in France or abroad, or from public or private research centers.

L'archive ouverte pluridisciplinaire **HAL**, est destinée au dépôt et à la diffusion de documents scientifiques de niveau recherche, publiés ou non, émanant des établissements d'enseignement et de recherche français ou étrangers, des laboratoires publics ou privés.

# **Strength measurement and rupture mechanisms of a micron thick nanocrystalline MoS<sub>2</sub> coating using AFM based micro-bending tests**

G. Colas<sup>1,2</sup>, P. Serles<sup>1</sup>, A. Saulot<sup>3</sup>, T. Filleter<sup>1</sup>

<sup>1</sup> Department of Mechanical and Industrial Engineering, University of Toronto, 5 King's college road, Toronto ON M5S 3G8, Canada

<sup>2</sup> FEMTO-ST institute - Department of Applied Mechanics, Univ. Bourgogne Franche-Comté, CNRS, 24 Chemin de l'Épitaphe, 25000 Besançon, France.

<sup>3</sup> Université de Lyon, LaMCoS, INSA-Lyon, CNRS UMR 5259, France

## **Abstract**

The present study focuses on the measurement of mechanical properties of a 1.1 μm thick nanocrystalline MoS<sub>2</sub> coating deposited by magnetron sputtering with a particular interest in the strength of the coating. Mechanical strength is one of the most important properties to best predict failure of the coating, especially in the case of dry contact lubricated systems in which the coating of interest is often used. An Atomic Force Microscope based micro-bending experiment was developed to measure the rupture strength of MoS<sub>2</sub> micro cantilever-beams directly milled in the coating using a Focused Ion Beam. Rupture strength of the MoS<sub>2</sub> coatings was measured to be  $728 \pm 88$  MPa. Comparisons with nanoindentation was used to validate the micro-bending technique via the statistically indifferent measurement of the Young's modulus:  $63.1 \pm 5.0$  GPa and  $64.5 \pm 4.0$  GPa respectively. In depth study of the fractured beam surface and the microstructure of the coating revealed that the surface roughness and the crystallite size can be directly correlated to the rupture pattern. The crack was additionally shown to propagate within the nanocrystalline

network existing in the coating. Parallels with the tribological behaviour of the coating are drawn and further confirm the lubrication mechanism described in previous studies.

**Keyword:**

MoS<sub>2</sub>, rupture strength, AFM bending test, focused ion beam, micro cantilever-beam

---

## **1 Introduction**

Micron thickness coatings deposited through highly controlled synthesis methods such as physical and chemical vapour deposition have demonstrated their suitability in a broad range of applications including lubrication [1,2], machining [3], nuclear energy [4], and high-speed electronics [5]. While these coatings exhibit favourable functionally driven properties in this wide range of applications, the understanding of their mechanical and structural characteristics remains, in many cases, limited. Of particular interest is the synthesis and characterization of MoS<sub>2</sub> coatings intended to be used in tribological applications. In literature, significantly different MoS<sub>2</sub> coating structures are observed due to wide variances in deposition methods such as direct-current or radio-frequency sputtering, and sputtering parameters such as chamber pressure and voltage [6–8]. Even the same deposition parameters have been shown to produce different coating structures during subsequent depositions due to variability in the system, sputtering target, or contaminants in the system [9]. This deposition variability directly influences the structure of MoS<sub>2</sub> coatings; ranging from highly organized columnar structures [6] to fully amorphous structures [10]. Studies on the mechanical properties of MoS<sub>2</sub> coatings also demonstrate a wide variance with Young's modulus and hardness values ranging from 50 to 170 GPa [3,10–12] and from 0.5 to 8 GPa [3,10–16] respectively. Furthermore, there is a limited number of studies on both the rupture and the fracture strength of

the coatings. Measurement of those properties can be done via scratch testing, however finite element modelling can be required to evaluate, from the experimental data, the stress intensity factor related to fracture strength of the coating material [17]. Precise knowledge of these parameters is very important for predicting coating failure through crack formation and propagation, because it ultimately leads to particle detachment and coating delamination.

Most commonly, mechanical properties of micron-thin coatings are determined using nanoindentation as it allows the measurement of hardness and Young's modulus with minimal sample preparation [18]. However, nanoindentation suffers from limitations linked to a number of instrument and material parameters including: material pile-up and sink-in, substrate and roughness effects, and system compliance which are known to strongly influence the measurement reliability [18]. To overcome these limitations, a new approach has emerged throughout the last 15 years; high-precision milling of microstructures using a Focused Ion Beam (FIB) and deflecting the structure through the use of nanoindentation techniques. These structures take a variety of shapes including: free standing films [19,20]; micro pillars [21–23]; or micro-bridges and micro-cantilever beams [4,23–29]. Of particular interest, micro-bending tests allow the study of several mechanical properties – Young's modulus, yield stress, strength, fracture toughness – relative to the specific crystal orientation [4,28], the substructure of hierarchical architectures [26], or as an average for the entire coating [4,27]. However, effective use of this technique requires high-resolution measurements of the deflection, the applied force, and an exact knowledge of the location of loading. Additionally, indenter penetration into the beam has to be considered as it can lead to significant error in deflection values [24,30]. While this leads to complications for nanoindenters and in situ Scanning Electron Microscope experiments (SEM), Atomic Force Microscopy (AFM) can be a good solution as higher resolution in force, deflection, and accurate

loading location can be achieved. Micro-bending tests using AFM on submicron beams fabricated by FIB [31] and chemical and wet etching processes [32–35] have allowed the study of stiffness, bending strength, fracture toughness, and even fatigue toughness of materials.

In the present study, micro-cantilevers beams prepared by FIB-milling a 1.1  $\mu\text{m}$  thick nanocrystalline  $\text{MoS}_2$  coating were subjected to bending tests using an AFM. Through the use of AFM deflection, high accuracy study of the Young's modulus, rupture strength, and structural fracture mechanism of the coating was conducted. The AFM micro-bending tests were additionally validated via static and continuous stiffness nanoindentation measurements. As well, to better understand the structural characteristics of the coating a Transmission Electron Microscopy (TEM) study of the coating cross-sectional microstructure was also performed.

## **2 Experiments**

### **2.1 Materials**

The material of focus is a  $1.10 \pm 0.01 \mu\text{m}$  thick  $\text{MoS}_2$  coating deposited by radio-frequency magnetron sputtering. The coating was sputtered on an N-doped Silicon wafer having a 285 nm thick  $\text{SiO}_2$  oxide layer. The coating is space-qualified, i.e. it passed all tests imposed by space agencies to be used in space, and it has been used for many years. It was deposited by Blösch AG., Grenchen, Switzerland.

This particular  $\text{MoS}_2$  coating has been previously described as a dense columnar-like nanocrystalline structure (fibrous and vertically oriented) [36] based on the cauliflower aspect of its surface, the deposition parameters, and fractured surfaces of delaminated portions [15,36–39]. Delamination and cracks have been observed under Scanning Electron Microscopy (SEM) and their features suggest that rupture likely occurs at the interface between grains/columns [38].

However, to the author's knowledge, there are neither studies on the rupture mechanism of such MoS<sub>2</sub> coatings nor reports of the strength of the interface between grains.

## **2.2 Micro-cantilever beam Preparation**

MoS<sub>2</sub> micro-cantilever beams were prepared using a Hitachi NB5000 high precision dual-beam FIB and SEM. In order to achieve micro-cantilever beams consisting of freestanding MoS<sub>2</sub>, the FIB-milling was performed without the protective metallic layer on the MoS<sub>2</sub> coating which is commonly used during FIB-milling. The beams were milled using a high-voltage Ga<sup>+</sup> gun in a three-stage process allowing for the creation of free-standing triangular cantilever beams as seen in Figure 1a. First, 3 rectangular volumes are removed using a high energy beam (40 kV, 19.5 nA) creating a rectangular structure of MoS<sub>2</sub> coating with one end connected to the bulk of the coating. Second, the undercut was performed at angles of either 45° or 58° on each side with a medium ion beam energy (40 kV, 3.8 nA). At this stage, re-deposition of material, primarily made of Si and Ga, accumulates on the undercut side of the micro-cantilever beam, therefore, a third low-energy (40 kV, 0.8 nA) slow cleaning cut was performed to remove this re-deposited layer (cf. SI 1). These beam energies were carefully selected to minimize the FIB induced damage and amorphization of the coating [40–43] (SI 2). In total 11 micro-cantilever beams were successfully characterized with dimensions varying from 9 to 15 μm in length, 1.4 to 2.2 μm in width, and 0.6 to 1.3 μm in height.

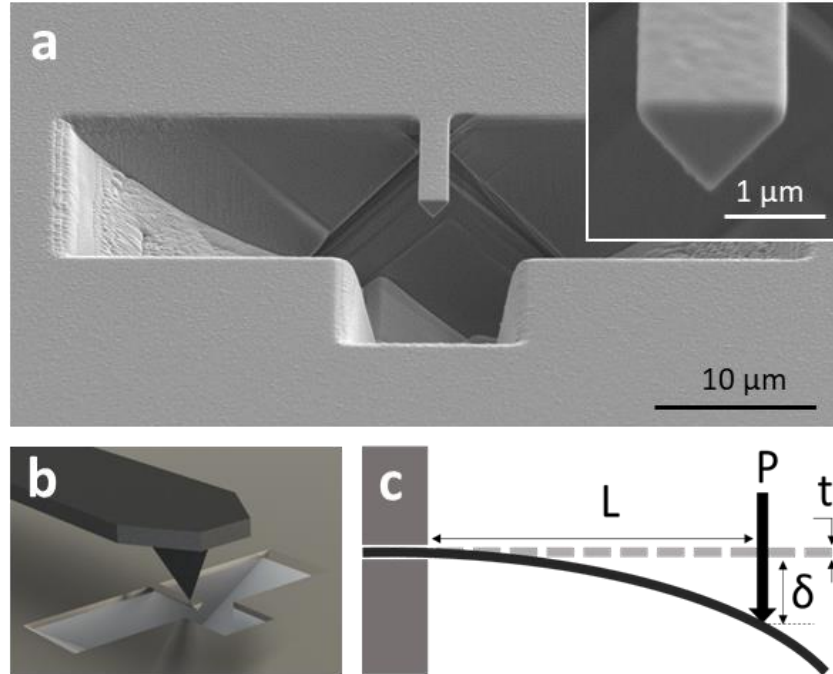


Figure 1 - (a) SEM image of a  $\text{MoS}_2$  micro-cantilever beam FIB milled in the  $1.1 \mu\text{m}$  thick  $\text{MoS}_2$  coating, the inset is a zoomed in image on the beam cross section. (b) 3D schematic representation of the bending test using AFM, at scale. (c) schematic of the deflection test performed on the beam using AFM.

### 2.3 AFM Micro-Bending Tests

Microbeam bending tests were performed using an Atomic Force Microscope (MFP-3D, Oxford Instruments; Asylum Research Ltd.) with sharp-tip ( $<10 \text{ nm}$  tip radius) silicon probes (cantilever with  $42 \text{ N/m}$  spring constant, calibrated geometrically) from Nano Sensors as represented in Figure 1b. The microbeams were first imaged in tapping mode AFM to position the cantilever after which the deflection tests were performed in a static deflection mode. On each  $\text{MoS}_2$  cantilever beam, the bending tests were performed in at least 3 different positions along the length of the beam, as recommended in [24]. The tip was positioned along the longitudinal axis at distances from the clamped end from  $6 \mu\text{m}$  to  $13 \mu\text{m}$  to ensure the validity of the Euler-Bernoulli deflection theory

[44]. At each location, incremental loading was performed from 0.5-10  $\mu\text{N}$  with 5 deflections at each load.

To create consistency between all beam sizes and loading conditions, the deflection test data was converted into a stress-strain curve using the same model as Bechtle et al. [26]. In the calculation of the beam deflection from the AFM measurements, no indentation depth correction was needed because the tip does not indent the coating by more than 10 nm at a load of 20 $\mu\text{N}$  for an equivalent beam deflection up to 800 nm. Equations (1) and (2) were used to calculate the stress  $\sigma$  and the strain  $\varepsilon$  respectively.  $P$  is the force applied at the loading point, located at a distance  $L$  from the clamped end.  $t$  represents the thickness of the beam,  $w$  the width, and  $\delta$  is the beam deflection, as schematized on Figure 1c. The coating is assumed to be macroscopically homogenous and assumed to exhibit isotropic mechanical properties.

$$\sigma = \frac{12*P*L}{w*t^2} \quad (1)$$

$$\varepsilon = \frac{\delta*t}{L^2} \quad (2)$$

The Young's modulus  $E$  is calculated based on the linear fit of the curves in the 0 to 0.1% strain range. The rupture strength  $R_m$  is determined as the stress at which the micro-cantilever beam fractures.

## 2.4 Surface, Microstructure, and Compositional Analysis

The FIB micro-cantilever beam structures were analyzed using SEM (Hitachi SU3500) and HRSEM (Hitachi SU5000) secondary electron imaging to determine beam dimensions and analyze the surfaces after fracture. The coating surface morphology was studied using AFM in tapping-mode. The characterization of the coating cross-section was performed using Transmission



Electron Microscopy (TEM) (Hitachi HF3300) and Scanning Transmission Electron Microscopy (STEM) to study the microstructure at the nanoscale using backscatter, bright-field, and dark-field micrographs. The TEM samples were prepared by a standard lift-out procedure using the same high precision FIB with Ga<sup>+</sup> ions accelerated to 40 kV. To preserve the structure of the MoS<sub>2</sub> coating during FIB cross-sectional lift-outs, a 0.5 μm thick tungsten layer was deposited on the coating prior to milling using ion beam plasma deposition from a WC<sub>2</sub> gas. Two samples of 65 nm and 76 nm in thickness respectively were examined in TEM and STEM using accelerating voltage and emission currents of 300 kV and 5 μA respectively.

## **2.5 Nanoindentation Tests**

The nanoindentation measurements were performed on an Anton Parr UNHT nanoindenter with a diamond Berkovich tip to evaluate the Young's modulus  $E$  and the Hardness  $H$  of the coating. In addition to mechanical characterization of the coating, the measurement of the Young's modulus (depth variation, and bulk values) was used to compare with the cantilever beam tests results. In total, 50 indentations were performed (two sets of 25) with the load pattern of: (1) load up to 500 μN at a speed of 3000 μN/min, (2) hold at 500 μN for 10 seconds to allow for stress relaxation, (3) unload the contact at rate of 3000 μN/min. The extraction of  $E$  and  $H$  parameters was done using the Oliver-Pharr method [45] considering a Poisson's ratio of 0.27 [46]. Additionally, 12 measurements in the Continuous Stiffness Measurement (CSM) nanoindentation mode were performed. CSM is a technique in which the indentation tip is continuously loaded and unloaded throughout the depth of indentation thereby generating  $E$  and  $H$  values incrementally throughout the depth [47,48]. To avoid instrument errors such as the woodpecker effect and low signal-to-noise ratio, CSM parameters of 300 μN/min loading rate, 40 μN sinusoidal amplitude, and

maximum load of 2 mN were selected [49]. The woodpecker effect refers to “the tip losing contact with the specimen during loading and unloading cycles during CSM” [49]. The surface function of the tip was re-calibrated before each set of measurements to ensure coherence. After indentation, the surface was imaged using the AFM in tapping mode to identify the effective contact area (material pile-up or sink-in around the indent) which is used in E and H calculations.

### **3 Results**

#### **3.1 Cross-Sectional Electron Microscopy Characterization**

The SEM image of the fractured coating cross-section (Figure 2a) shows a dense microstructure with roughly vertically oriented grains. These grains appear to be in accordance with the dark field STEM micrograph (Figure 2b) where large light gray vertically oriented regions of similar magnitude are delimited by thin dark frontiers. The high-resolution STEM images (Figure 2 c,d,e) show three distinct phases vertically distributed within the coating. The surface  $47 \pm 5$  nm exhibits a purely amorphous phase (Figure 2c) while the central bulk of the coating exhibits a nanocrystalline phase embedded in an amorphous matrix (Figure 2d). These bulk nanocrystals are vertically oriented within  $\pm 28^\circ$  of the vertical axis and represent approximately 35% of the total volume. Across 10 micrographs studied, a total of 189 nanocrystals were identified with widths of  $13.1 \pm 1.1$  atomic layers ( $8.1 \pm 2$  nm;  $c_{\text{MoS}_2} = 6.15 \text{ \AA}$  [50]) in the [001] direction and lengths of  $12 \pm 4$  nm in the [100] or [010] directions. The third phase exists as the bottom interface of the coating with a height of  $17 \pm 4$  nm and consists of similarly sized nanocrystals in an amorphous matrix as in the bulk, but horizontally oriented within  $\pm 22^\circ$  of the horizontal axis as seen in Figure 2e.

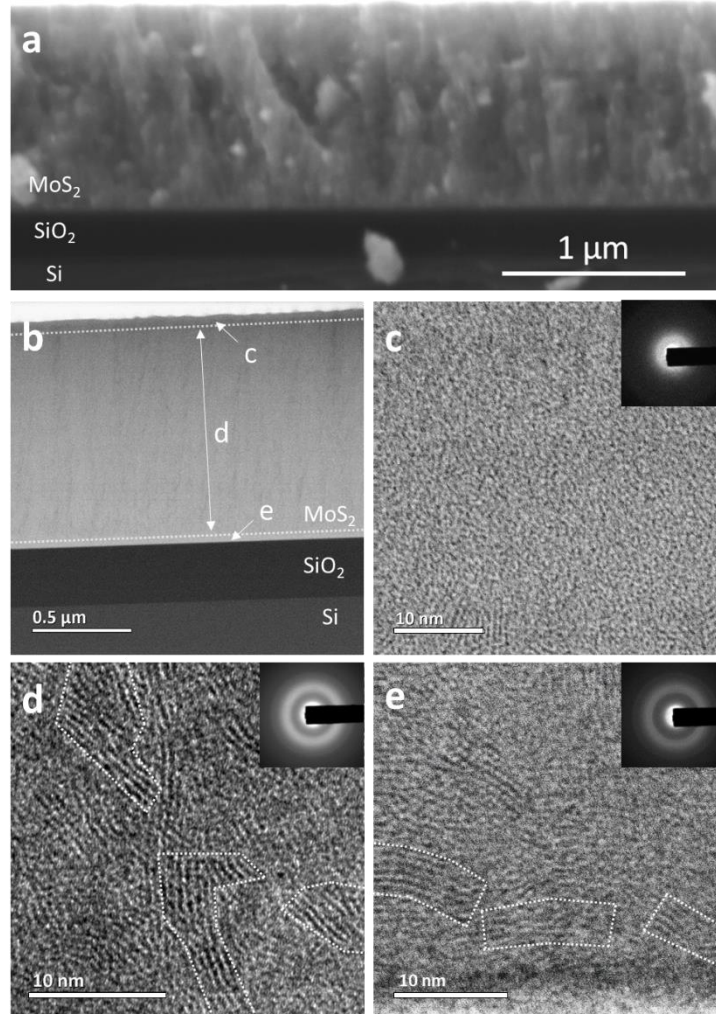


Figure 2 - (a) SEM image of the fractured cross-section of MoS<sub>2</sub> coating. (b) to (e) TEM images of the coating cross-section; (b) low magnification dark field image of the entire coating thickness with a small portion of the wafer substrate; (c) high magnification image of the coating top surface showing an amorphous structure; (d) high magnification image of the coating bulk showing vertically aligned crystallites; and (e) high magnification image showing the horizontally aligned crystallites at the bottom interface with the SiO<sub>2</sub> layer.

### 3.2 Nanoindentation

50 static mode indentations were conducted in two sets of 25 with indentation depths of  $59 \pm 1$  nm and  $43 \pm 4$  nm respectively, both below the 10% thickness limit recommended for thin film characterization [18]. The average Young's modulus and hardness for this MoS<sub>2</sub> coating obtained from the all 50 measures were found to be  $E = 63.1 \pm 5$  GPa and  $H = 4.0 \pm 0.7$  GPa respectively

with no significant difference between the two measurement sets. The indentation loading curves show a plateau when the load is maintained constant at 500  $\mu\text{N}$  for 10s (Figure 3a). This plateau is the effect of stress-induced creep which can be linked to viscoelasticity or viscoplasticity in the material [18]. During unloading, the curve demonstrates hysteresis with a different slope as compared to the loading curve (Figure 3a). However, surprisingly, the AFM topographic study of the indented regions shows no significant indent (Figure 3b). To ensure proper location, one indent at 2 mN load was performed at known distances from the 500  $\mu\text{N}$  indents. Note that no significant material pile-up or sink-in is detected in and around the high load indent (Figure 3b). The two sets of 25 indentations which were performed show differences that are attributed to rounding of the Berkovich tip between the measurements as evidenced by changes in the calibrated tip function (cf. SI 3).

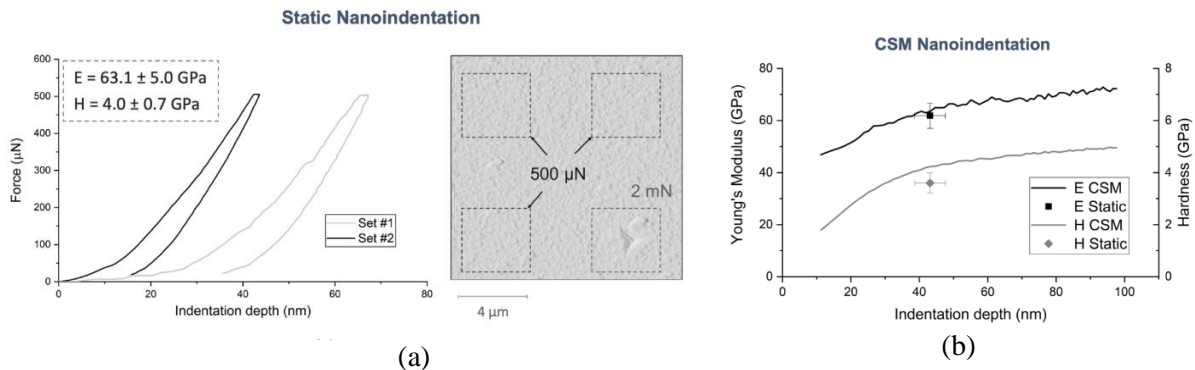


Figure 3 – (a) Examples of static mode indentation curves from the 1<sup>st</sup> and 2<sup>nd</sup> set of 25 indents and AFM image of the surface after indentation; inset on the indentation curve gives the calculated values of E and H over the 50 indents. (b) Example of CSM data obtained on pristine MoS<sub>2</sub>, average value from the 2<sup>nd</sup> set of 25 indents from static mode indentation is shown for comparison.

The indentations performed in CSM mode (Figure 3b) were considered only up to an indentation depth of 100 nm (<10% coating thickness) and the first 10 nm of indentation was negated due to noise from the woodpecker effect. Interestingly, the MoS<sub>2</sub> sample shows an increasing trend for E and H values with respect to the indentation depth, in particular at depths below  $\sim 45$  nm. As well,

for E there exists a transition from nonlinear to linear which corresponds with approximately 45 nm of depth. In comparison to the second set of static indentations (same tip function as in CSM mode), at 43 nm of depth (corresponding to 500  $\mu\text{N}$  load) both the E and H values are consistent with the static mode values as reported in the inset of the graph on Figure 3a.

### 3.3 Micro-bending tests

The rupture strength ( $R_m$ ) values for the five micro-cantilever beams that were successfully fractured as well as the values of Young's modulus (E) measured from nine beams are presented in Table 1. The results show very consistent E values across the beams giving  $E = 64.5 \pm 4.0$  GPa. Beam #10 demonstrated an AFM tip-sliding event (cf. SI 4) which might have modified the tip/beam interface (e.g. transfer of material to the tip). This may explain the strong non-linearity observed during the first 1% strain and consequently the outlier E value of  $81.7 \pm 4.5$  GPa; beam #10 was thus removed from the E average. As discussed in SI 5, contrary to E, the  $R_m$  of beam #5 does not appear to be as sensitive to the redeposition.  $R_m$  indeed stays within the range of values defined by the other beams. Considering this additional  $R_m$  value to the five presented in **Table 1**, the average value is  $R_m = 728 \pm 88$  MPa. Although both E and  $R_m$  exhibit values within a reasonably narrow range across the six beams considered, two groups tend to be observed if the strain to rupture is considered. Indeed, four beams (#3, #5, #7 and #9) exhibit a strain to rupture in the 1.2% - 1.3% range while beams #8 and #10 exhibit a strain to rupture higher than 2.4% as seen in Figure 4a.

Table 1 - Young's modulus (E), rupture strength (Rm) and geometry of the micro beams measured using AFM micro beam deflection testing.

Beam #	Width (μm)	Height (μm)	E (GPa)	Rm (MPa)
1	2.2	1.1	67.3 ± 1.5	-
2	1.5	0.76	59.7 ± 3.5	-
3	1.5	0.8	67.2 ± 2.5	740
6	1.5	0.83	65.7 ± 3.7	-
7	1.75	1.23	71.7 ± 1.9	810
8	1.64	1.16	61.7 ± 5.0	810
9	1.88	1.35	61.1 ± 3.8	570
10	1.78	1.29	81.7 ± 4.5	710
11	1.4	0.63	65.3 ± 3.7	-

Regarding the fracture mode, the stress/strain curves (Figure 4a) demonstrate that the coating is brittle as the beams exhibit no plasticity prior to fracture, which is confirmed by the HRSEM images of the fractured surface (Figure 4b & c). While the stress/strain curve of beam #10 shows strong non-linearity over the first 1% strain, the fracture surface is identical to the fracture surface shown in Figure 4b which furthers the assumption that Rm is independent of E for these beams. All the fracture surfaces show a multi-faceted structure within the coating bulk; the fracture plane is not a single shear plane but rather made of many smaller fracture surfaces. Additionally, a different contrast between the top 50 nm and the bulk of the coating within the beam is clearly observable in SEM as shown on Figure SI 2 which demonstrates a change in the coating structure locally within that thickness, consistent with TEM observations. Finally, there exists a clear transition in the topography of the fracture surface with a step at approximately half of the height from the top surface. There is a  $90^\circ < \alpha < 120^\circ$  shift in propagation direction of the cracks over

few hundred nm distance around half the beam thickness before the second straight brittle fracture finally occurs.

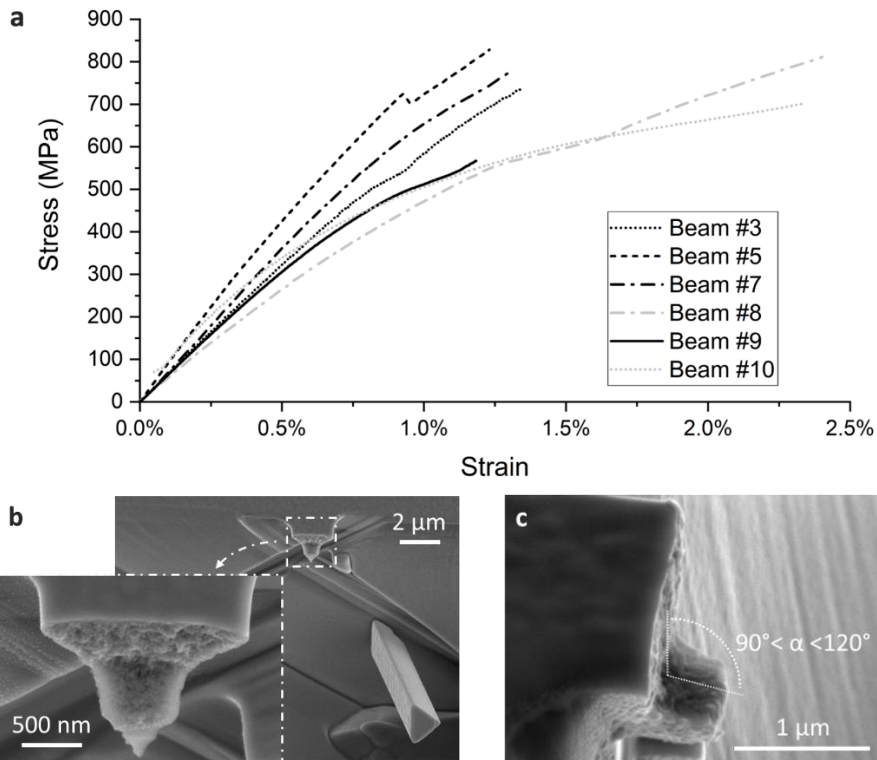


Figure 4 - (a) Stress/strain curves up to fracture of the beams on which rupture strength has been measured, (b) & (c) fracture surface of the beam at the clamped end

## 4 Discussions

### 4.1 Stiffness & Ductility

Great consistency is observed between the indentation tests and the microbeam deflection tests, which validates the AFM based deflection method. Both evaluation methods independently show a Young's modulus of approximately 64 GPa which compares well with the range of 50-170 GPa reported in literature for MoS<sub>2</sub> coatings [10–12]. This good correlation between both measurement techniques supports the two major assumptions that were made in determining the Young's modulus. First, the assumption of isotropic mechanical properties through the entirety of the coating which was made for the microbeams is validated as it provides a statistically indifferent E

value to nanoindentation which interacts only with the surface volume rather than the entire volume. Second, the strong correlation between the results obtained by the two independent techniques indirectly validates that the Poisson ratio for MoS<sub>2</sub> is  $\nu = 0.27$ . This value of Poisson's ratio is, to the authors' knowledge, the only reported value measured for MoS<sub>2</sub> and is the result of a single crystal study conducted 40 years ago [46]. In the present study, only the nanoindentation calculation uses the Poisson's ratio to determine E while the microbeam deflection is independent of this value thus indirectly confirming the validity.

The CSM measurements for the MoS<sub>2</sub> coating show a nonlinear increasing trend for E which is characteristic of porous materials response to such loading [51–53]. This supports well the already suspected presence of porosities due to significant gas desorption during friction of the same coating [36,54]. Since porosity promotes crack propagation, this further suggests that this is a low-ductility brittle coating [55,56].

While the nanoindentation and micro-cantilever beam techniques provide statistically indifferent values for E, as the micro-cantilever beams were FIB-milled without the protective tungsten layer on the coating, concern of Ga<sup>+</sup> ion induced amorphization was considered. In order to identify if this occurred during the micro-cantilever beam manufacturing, two studies were performed to compare the pristine coating to the area immediately surrounding the microbeam structures (SI 2). Both investigations presented statistically indifferent results between the microbeam region and the pristine coating, which suggests that the stray Ga<sup>+</sup> ions in the present study had a negligible impact on the microbeam evaluations.



## 4.2 Hardness

Regarding the hardness, the static nanoindentation results present a medium-high hardness value of 4.0 GPa compared to 0.5-8 GPa for MoS<sub>2</sub> coatings in literature [10–16]. This is likely due to the nanocrystalline structure of the coating in accordance with the Hall-Petch effect [57]; the high concentration of grain boundaries in nanocrystalline materials inhibit dislocation movement which provides a material with high hardness and low ductility [58]. Although the nanocrystals are embedded in an amorphous matrix, the hardness is nonetheless expected to be high as the crystallites were measured to be  $12 \pm 4$  nm in length which represents nearly the smallest size and therefore maximum hardness before the breakdown of the Hall-Petch relationship [59]. Interestingly, while clear energy dissipation (usually linked to plasticity) is observed during static mode indentation, no residual imprint was found (Figure 3a). Stempflé et al. noted the same effect in indentation of graphite based 3<sup>rd</sup> body [60] and suggested that “the deformation energy during the indentation is partly dissipated by structural changes of the elemental particles”. It is known that under compression and shear stress (i.e. friction) amorphous MoS<sub>2</sub> based material can crystallize into crystalline MoS<sub>2</sub> [61–63]. However, it could not be verified in the shallow indentation case as studied here. Another assumption might be that the surface is able to elastically recover while the stresses are transferred into the subsurface bulk of the coating. In the MoS<sub>2</sub> case studied here, there is a plateau during the time the load is kept constant, which means the indenter continues penetrating in the material. This, in combination with the observed lack of indent detected on the surface, suggests that the MoS<sub>2</sub> coating is either demonstrating viscoelastic properties or slow structural rearrangement such as the recrystallization mentioned above.

Such a behaviour could explain the low linear increase in hardness observed past the 45 nm indentation depth. Altogether, evidence supports material “reconfiguration” rather than visco-elasticity/plasticity.

### **4.3 Rupture Strength & Fracture**

For six of the microbeams, deflection until fracture was achieved which ultimately demonstrated brittle failure of the MoS<sub>2</sub> coating. The resulting rupture strength provides a comparable value to the MoS<sub>2</sub> yield stress measured during nano-compression tests reported as  $821 \pm 141$  MPa [64]. For a material exhibiting a brittle failure such as this, yield would result right before rupture, which occurs at  $R_m = 728 \pm 88$  MPa in the present case. Additionally, the brittle fracture pattern of the coating observed after the micro-bending rupture tests is consistent with the nano-indentation results which suggest a brittle response of the MoS<sub>2</sub> coating. This is also consistent with observations from tribological tests during which brittle failure of the coating with partial delamination has been seen [38]. Interestingly, results can be divided into two classes based on the strain to failure. No clear explanation for these two regimes was found except for inherent heterogeneities within the coating.

The multi-faceted morphology shown in the HRSEM images of the fracture surfaces (Figure 4b) is consistent with the idea of a nanocrystalline structure within the coating; the crack propagation within the coating would follow an intergranular fracture pattern along the variably oriented nanocrystallites thus providing a multi-faceted morphology as seen herein. Additionally, the general direction of fracture isn't straight but presents two fracture directions oriented at  $90^\circ < \alpha < 120^\circ$  to each other. The transition between the two directions is a clear step located approximately half of the thickness below the top surface of the beam. This location is slightly

below the theoretical neutral bending axis of a triangular prism, which divides the tensile and compressive regimes above and below the neutral axis respectively. Similar fracture surface morphology has been seen in the past for similar scale tests on Si, which corresponded to the neutral bending axis [32]. Additionally, in porous brittle material, it has been shown that while tensile stress creates unstable crack propagation leading to catastrophic failure, the propagation quickly stabilizes under compressive stress and is rather contained [56]. However, in the MoS<sub>2</sub> case studied herein, a difference in compressive regime versus tensile regime may not solely explain such unusual fracture surface. The shift in crack propagation at half the beam height however corresponds to the location of maximum shear stress, which would suggest that the bulk of the MoS<sub>2</sub> coating is sensitive to rupture by shear stress, even if the TEM appears to show vertically aligned crystallites.

If Griffith's theory is considered, it is possible to link the fracture stress to the crack length thanks to equation (3). If  $R_m$  is used as the fracture stress  $\sigma_f$  and either the specific surface energy of MoS<sub>2</sub> (0.11 Nm<sup>-1</sup>) or the interlayer binding energy of MoS<sub>2</sub> layers (0.22 Nm<sup>-1</sup>) [65] are used as values for the surface energies of the crack  $\gamma$ , then the crack length  $a$  determined from equation (3) is within the 9 nm to 16 nm range. These values are consistent with peak-to-valley distances measured on the top surface roughness of the beam (cf. SI 6), which was also demonstrated in the Si microbeam case [32]. The roughness would thus act as a pre-crack. That means roughness can most likely be at the origin of crack initiation, with the crack propagating within the MoS<sub>2</sub> crystallites or at the interface between them.

$$\sigma_f = \sqrt{\frac{2\gamma E}{\pi a}} \quad (3)$$

It has been shown that friction between crystallites occurs due to the rupture of weak points at the inter-crystallite interface [66]. Moreover, tests performed on 2D MoS<sub>2</sub> crystals show that interlayer

sliding during bending occurs only when the number of layers is higher than 10 [65] while the TEM study shows that nanocrystallites comprising the MoS<sub>2</sub> coating studied herein are made of  $13.1 \pm 1.1$  atomic layers on average. As a result, combination of soft interface fracture at the interface between the nanocrystallites and interlayer sliding within the nanocrystallites is the most likely to happen.

As a consequence of several different internal mechanisms, it is proposed that the rupture mechanism of the micro-cantilever beam fabricated in the MoS<sub>2</sub> coating is most likely a combination of different phenomena governed by the roughness for crack initiation, the internal porosities, and the nanocrystalline network for crack propagation until failure. The sensitivity to shear stress (horizontal crack propagation in lower half) is suspected to be associated with crystallite reconfiguration via possible reorientation of crystallites after rupture of weak points at the inter-crystallite interface [66]. The morphology of the sheared surface appears flatter than, and not as multifaceted as, the other two straight parts of the fractured surfaces.

#### **4.4 Implications for Tribological Behaviour**

During previous studies, the MoS<sub>2</sub> coating studied herein has been tested as a dry lubricant coating, which is one of its primary uses. The mechanical characterization conducted in the present study plays a key role in better understanding the tribological behavior of this lubricant. The noted nanocrystalline structure aids in explaining why this lubricant performs better than purely amorphous coatings [1] or much harder coatings (H=8 GPa) [15]. The present study demonstrates that the coating can resist compressive stresses more than tensile stresses as the nanocrystalline network and porosities deter crack propagation throughout in the bulk under compression. Therefore, during normal compressive loading, the coating will not crack as quickly. When sliding

occurs, shear can generate both tensile and compressive regimes in the coating. Due to the crystalline and the porous networks coupled with sensitivity to shear stress, the propagation of the fracture can easily, and quickly, shift direction from perpendicular to the friction track to parallel to it without the crack propagating deep in the bulk. As the structure in the bulk of the coating is comprised of grains of small size, such behavior could most likely lead to small particle detachment. This ability to “feed” the contact by detaching small enough particles to be trapped in the contact and lubricate it is the mechanism of 3<sup>rd</sup> body formation proposed in the previous tribological studies performed on this specific coating [1,38]. Within all their MoS<sub>2</sub> coatings, Vierneusel et al. [15] obtained the best friction performances from a coating whose (i) surface exhibits similar surface morphologies to the coating studied here, and (ii) hardness and microstructure description that matches the present coating. However, TEM showed the presence of a 47 nm thick amorphous layer on top of the coating. This does not affect the scenario established above because under compression and shear, MoS<sub>2</sub> can recrystallize [61–63].

## **5 Summary & Conclusion**

This study focuses on the measurement of the rupture strength of a 1.1 μm thick nanocrystalline MoS<sub>2</sub> coating deposited by magnetron sputtering. An experimental protocol to perform bending tests using AFM on triangular FIB-milled micro-cantilever beams has been developed to characterize the mechanical properties of the coating. Alongside the micro-cantilever beams, an in-depth analysis of the mechanical properties and rupture behaviour under bending conditions was performed in conjunction with mechanical and structural analysis using nanoindentation, SEM, and TEM instruments. Better understanding of the tribological behavior identified in previous studies was thus possible. Furthermore, it is consistent with the assumed, but not

concretely proven, mechanisms of particle detachment in the 3<sup>rd</sup> body creation that is leading to the success of the lubrication.

For the first time, the rupture strength of the MoS<sub>2</sub> coating is measured to be  $R_m = 728 \pm 88$  MPa. The micro-bending tests also confirm the brittle nature of the coating, which was indirectly expected based on wear mechanisms observed in previous friction tests. The micro-bending tests combined with nanoindentation and microstructural studies using TEM demonstrated both the nanocrystalline and porous structure of the coating. Comparison with nanoindentation test results additionally validated the microbeam deflection technique as the Young's modulus determined independently with both techniques presents statistically indifferent results:  $63.1 \pm 5.0$  GPa and  $64.5 \pm 4.0$  GPa respectively. This sets an overall average value of  $E = 63.8 \pm 5$  GPa. Additionally, the consistency in the Young's modulus measured with both techniques allows for the confirmation that the Poisson's ratio value of  $\nu = 0.27$  is accurate for MoS<sub>2</sub>.

This study has consequently determined both the microstructural (crystallinity, grain shape and size, presence of porosity) and mechanical properties ( $E$ ,  $H$ ,  $R_m$ ,  $\nu$ ) of this MoS<sub>2</sub> coating thus presenting a near-complete understanding of the coating for tribological testing. It also demonstrated the influence of surface roughness and crystallite size in the coating resistance to fracture. This therefore sets the groundwork for future studies such as numerical simulation of the tribological behavior of the coating, structural compatibility with other thin-films for applications such as batteries and semi-conductors, and microstructural understanding for applications such as flexible electronics and nuclear energy.

## **Appendix**

Information and DOI for our SI

## Acknowledgement

The authors acknowledge support from the National Science and Engineering Research Council of Canada (NSERC), the Erwin Edward Hart Professorship, the Connaught Fund at the University of Toronto and the Canadian Foundation for Innovation (CFI). The authors would like to thank the Ontario Centre for the Characterization of Advanced Materials (OCCAM) and especially Sal Boccia and Jason Tam for their help in FIB-milling the micro-beams, FIB sample preparation for TEM, and TEM characterization; Prof. C.V. Singh as well as Eric Nicholson from the Material Science and Engineering Department of the University of Toronto for access and technical support with the nanoindenter.

## Funding

The National Sciences and Engineering Research Council of Canada;

The Ontario Ministry of Research and Innovation Early Researcher Award; the Erwin Edward Hart Endowed Professorship; Canadian Foundation for Innovation

## References

- [1] G. Colas, A. Saulot, E. Regis, Y. Berthier, Investigation of crystalline and amorphous MoS<sub>2</sub> based coatings: Towards developing new coatings for space applications, *Wear*. 330–331 (2015) 448–460. doi:10.1016/j.wear.2015.01.011.
- [2] C. Wang, B. Li, X. Ling, J. Zhang, Superlubricity of hydrogenated carbon films in a nitrogen gas environment: adsorption and electronic interactions at the sliding interface, *RSC Adv.* 7 (2017) 3025–3034. doi:10.1039/C6RA25505A.
- [3] W.H. Kao, Tribological properties and high speed drilling application of MoS<sub>2</sub>-Cr coatings, *Wear*. 258 (2005) 812–825. doi:10.1016/j.wear.2004.09.045.
- [4] X. Zhao, R.M. Langford, J. Tan, P. Xiao, Mechanical properties of SiC coatings on spherical particles measured using the micro-beam method, *Scr. Mater.* 59 (2008) 39–42. doi:10.1016/j.scriptamat.2008.02.022.
- [5] R.A. Street, Thin-film transistors, *Adv. Mater.* 21 (2009) 2007–2022. doi:10.1002/adma.200803211.
- [6] J. Moser, F. Levy, Crystal Reorientation and Wear Mechanisms in MoS<sub>2</sub> Lubricating Thin-Films Investigated By TEM, *J. Mater. Res.* 8 (1993) 206–213. doi:10.1557/jmr.1993.0206.
- [7] J. Moser, F. Levy, Growth Mechanisms and Near-Interface Structure in Relation To Orientation of MoS<sub>2</sub> Sputtered Thin-Films, *J. Mater. Res.* 7 (1992) 734–740. doi:10.1557/jmr.1992.0734.

- [8] J.M. Martin, H. Pascal, C. Donnet, T. Le Mogne, J.L. Loubet, T. Epicier, Superlubricity of MoS<sub>2</sub>: crystal orientation mechanisms, *Surf. Coat. Technol.* 68 (1994) 427–432.
- [9] D.G. Teer, V. Bellido-Gonzales, H. Hampshire, Molybdenum-Sulphur Coatings, US PATENT 6423419, 2002.
- [10] X. Wang, Y. Xing, S. Ma, X. Zhang, K. Xu, D.G. Teer, Microstructure and mechanical properties of MoS<sub>2</sub>/titanium composite coatings with different titanium content, *Surf. Coatings Technol.* 201 (2007) 5290–5293. doi:10.1016/j.surfcoat.2006.07.124.
- [11] N.M. Renevier, V.C. Fox, D.G. Teer, J. Hampshire, Properties of sputter-deposited MoS<sub>2</sub>/metal composite coatings deposited by closed field unbalanced magnetron sputter ion plating, *Surf. Coatings Technol.* 127 (2000) 24–37.
- [12] T. Le Mogne, C. Donnet, J.M. Martin, A. Tonck, N. Millard-Pinard, S. Fayeulle, N. Moncoffre, Nature of super-lubricating MoS<sub>2</sub> physical vapor deposition coatings, *J. Vac. Sci. Technol. A Vacuum, Surfaces, Film.* 12 (1994) 1998–2004. doi:10.1116/1.578996.
- [13] S. Watanabe, J. Noshiro, S. Miyake, Tribological characteristics of WS<sub>2</sub>/MoS<sub>2</sub> solid lubricating multilayer films, *Surf. Coatings Technol.* 183 (2004) 347–351. doi:10.1016/j.surfcoat.2003.09.063.
- [14] J. V. Pimentel, T. Polcar, A. Cavaleiro, Structural, mechanical and tribological properties of Mo-S-C solid lubricant coating, *Surf. Coatings Technol.* 205 (2011) 3274–3279. doi:10.1016/j.surfcoat.2010.11.043.
- [15] B. Vierneusel, S. Tremmel, S. Wartzack, Effects of deposition parameters on hardness and lubrication properties of thin MoS<sub>2</sub> films, *Materwiss. Werksttech.* 43 (2012) 1029–1035. doi:10.1002/mawe.201200942.
- [16] M. Simmonds, A. Savan, E. Pflüger, H. Van Swygenhoven, Mechanical and tribological performance of MoS<sub>2</sub> co-sputtered composites, *Surf. Coatings Technol.* 126 (2000) 15–24. doi:10.1016/S0257-8972(00)00521-1.
- [17] K. Holmberg, H. Ronkainen, A. Laukkanen, K. Wallin, S. Hogmark, S. Jacobson, U. Wiklund, R.M. Souza, P. Stähle, Residual stresses in TiN, DLC and MoS<sub>2</sub> coated surfaces with regard to their tribological fracture behaviour, *Wear.* 267 (2009) 2142–2156. doi:10.1016/j.wear.2009.01.004.
- [18] A.C. Fischer-Cripps, Nanoindentation, 2011. doi:10.1007/978-1-4419-9872-9.
- [19] C.J. Shute, J.B. Cohen, Determination of yielding and debonding in Al-Cu thin films from residual stress measurements via diffraction, *J. Mater. Res.* 6 (1991) 950–956. doi:10.1557/JMR.1991.0950.
- [20] Y. Xiang, X. Chen, T.Y. Tsui, J.I. Jang, J.J. Vlassak, Mechanical properties of porous and fully dense low- $\kappa$  dielectric thin films measured by means of nanoindentation and the plane-strain bulge test technique, *J. Mater. Res.* 21 (2006) 386–395. doi:10.1557/jmr.2006.0045.
- [21] P. Stoyanov, R. Merz, P.A. Romero, F.C. Wa, O.T. Abad, R. Gralla, P. Stemmer, M. Kopnarski, M. Moseler, R. Bennewitz, M. Dienwiebel, Surface Softening in Metal À Ceramic Sliding Contacts : An Experimental and Numerical Investigation, (2015) 1478–1491. doi:10.1021/nn505968m.
- [22] A.M. Korsunsky, M. Sebastiani, E. Bemporad, Residual stress evaluation at the micrometer scale: Analysis of thin coatings by FIB milling and digital image correlation, *Surf. Coatings Technol.* 205 (2010) 2393–2403. doi:10.1016/j.surfcoat.2010.09.033.
- [23] T. Schwark, O. Kraft, R. Schwaiger, The boundaries of soft magnetic composites reveal their complexity in compression and bending tests at the micro-scale, *Mater. Sci. Eng. A.* 684 (2017) 270–274. doi:10.1016/j.msea.2016.12.056.



- [24] S. Massl, W. Thomma, J. Keckes, R. Pippan, Investigation of fracture properties of magnetron-sputtered TiN films by means of a FIB-based cantilever bending technique, *Acta Mater.* 57 (2009) 1768–1776. doi:10.1016/j.actamat.2008.12.018.
- [25] M. Sebastiani, C. Eberl, E. Bemporad, G.M. Pharr, Depth-resolved residual stress analysis of thin coatings by a new FIB-DIC method, *Mater. Sci. Eng. A.* 528 (2011) 7901–7908. doi:10.1016/j.msea.2011.07.001.
- [26] S. Bechtle, H. Ozcoban, E.T. Lilleodden, N. Huber, a. Schreyer, M. V. Swain, G. a. Schneider, Hierarchical flexural strength of enamel: transition from brittle to damage-tolerant behaviour, *J. R. Soc. Interface.* 9 (2012) 1265–1274. doi:10.1098/rsif.2011.0498.
- [27] D. Di Maio, S.G. Roberts, Measuring fracture toughness of coatings using focused-ion-beam-machined microbeams, *J. Mater. Res.* 20 (2005) 299–302. doi:doi:10.1557/JMR.2005.0048.
- [28] F. Iqbal, J. Ast, M. Göken, K. Durst, In situ micro-cantilever tests to study fracture properties of NiAl single crystals, *Acta Mater.* 60 (2012) 1193–1200. doi:10.1016/j.actamat.2011.10.060.
- [29] J. Schaufler, C. Schmid, K. Durst, M. G??ken, Determination of the interfacial strength and fracture toughness of a-C:H coatings by in-situ microcantilever bending, *Thin Solid Films.* 522 (2012) 480–484. doi:10.1016/j.tsf.2012.08.031.
- [30] W. a Sasangka, C.L. Gan, D. Lai, C.S. Tan, C. V Thompson, Characterization of the Young's modulus, residual stress and fracture strength of Cu–Sn–In thin films using combinatorial deposition and micro-cantilevers, *J. Micromechanics Microengineering.* 25 (2015) 035023. doi:10.1088/0960-1317/25/3/035023.
- [31] D. Lu, A.H. Barber, Optimized nanoscale composite behaviour in limpet teeth, *J. R. Soc. Interface.* 9 (2012) 1318–1324. doi:10.1098/rsif.2011.0688.
- [32] T. Namazu, Y. Isono, T. Tanaka, Evaluation of size effect on mechanical properties of single crystal silicon by nanoscale bending test using AFM, *J. Microelectromechanical Syst.* 9 (2000) 450–459. doi:10.1109/84.896765.
- [33] S. Sundararajan, B. Bhushan, Development of AFM-based techniques to measure mechanical properties of nanoscale structures, *Sensors Actuators A.* 101 (2002) 338–351.
- [34] D. Choi, J. Jeon, P. Lee, W. Hwang, K. Lee, H. Park, Young's modulus measurements of nanohoneycomb structures by flexural testing in atomic force microscopy, *Compos. Struct.* 79 (2007) 548–553. doi:10.1016/j.compstruct.2006.02.023.
- [35] W. Sumelka, T. Blaszczyk, C. Liebold, Fractional Euler-Bernoulli beams: Theory, numerical study and experimental validation, *Eur. J. Mech. A/Solids.* 54 (2015) 243–251. doi:10.1016/j.euromechsol.2015.07.002.
- [36] G. Colas, A. Saulot, C. Godeau, Y. Michel, Y. Berthier, Decrypting third body flows to solve dry lubrication issue - MoS<sub>2</sub> case study under ultrahigh vacuum, *Wear.* 305 (2013) 192–204. doi:10.1016/j.wear.2013.06.007.
- [37] P.D. Fleischauer, M.R. Hilton, R. Baur, Effects of microstructure and adhesion on performance of sputter-deposited MoS<sub>2</sub> solid lubricant coatings, 1990.
- [38] G. Colas, Utilisation raisonnée de contaminants pour caractériser la rhéologie des 1ers et 3ème corps solides : Application à la tribologie en ambiances spatiales, INSA de Lyon, 2013. <https://tel.archives-ouvertes.fr/tel-00961216/>.
- [39] J. Moser, Composition and growth mode of MoS<sub>x</sub> sputtered films, *J. Vac. Sci. Technol. A Vacuum, Surfaces, Film.* 12 (1994) 494. doi:10.1116/1.579157.
- [40] F. Hofmann, E. Tarleton, R.J. Harder, N.W. Phillips, P.-W. Ma, J.N. Clark, I.K. Robinson,

- B. Abbey, W. Liu, C.E. Beck, 3D lattice distortions and defect structures in ion-implanted nano-crystals, *Sci. Rep.* 7 (2017) 45993. doi:10.1038/srep45993.
- [41] D. Kiener, C. Motz, M. Rester, M. Jenko, G. Dehm, FIB damage of Cu and possible consequences for miniaturized mechanical tests, *Mater. Sci. Eng. A.* 459 (2007) 262–272. doi:10.1016/j.msea.2007.01.046.
- [42] M.B. Lowry, D. Kiener, M.M. Leblanc, C. Chisholm, J.N. Florando, J.W. Morris, A.M. Minor, Achieving the ideal strength in annealed molybdenum nanopillars, *Acta Mater.* 58 (2010) 5160–5167. doi:10.1016/j.actamat.2010.05.052.
- [43] S. Rubanov, P.R. Munroe, FIB-induced damage in silicon, *J. Microsc.* 214 (2004) 213–221. doi:10.1111/j.0022-2720.2004.01327.x.
- [44] S.K. Park, X.L. Gao, Bernoulli-Euler beam model based on a modified couple stress theory, *J. Micromechanics Microengineering.* 16 (2006) 2355–2359. doi:10.1088/0960-1317/16/11/015.
- [45] W.C. Oliver, G.M. Pharr, An improved technique for determining hardness and elastic modulus using load and displacement sensing indentation experiments, *J. Mater. Res.* 7 (1992) 1564–1583.
- [46] J.L. Feldman, Elastic constants of 2H-MoS<sub>2</sub> and 2H-NbSe<sub>2</sub> extracted from measured dispersion curves and linear compressibilities, *Solid State Commun.* 19 (1976) viii. doi:10.1016/0038-1098(76)90082-X.
- [47] X. Li, B. Bhushan, A review of nanoindentation continuous stiffness measurement technique and its applications, *Mater. Charact.* 48 (2002) 11–36. doi:10.1016/S1044-5803(02)00192-4.
- [48] J. Hay, P. Agee, E. Herbert, Continuous stiffness measurement during instrumented indentation testing, *Exp. Tech.* 34 (2010) 86–94. doi:10.1111/j.1747-1567.2010.00618.x.
- [49] G.M. Pharr, J.H. Strader, W.C. Oliver, Critical issues in making small-depth mechanical property measurements by nanoindentation with continuous stiffness measurement, *J. Mater. Res.* 24 (2009) 653–666. doi:10.1557/jmr.2009.0096.
- [50] X. Li, H. Zhu, Two-dimensional MoS<sub>2</sub>: Properties, preparation, and applications, *J. Mater.* 1 (2015) 33–44. doi:10.1016/j.jmat.2015.03.003.
- [51] D. Jauffrès, C. Yacou, M. Verdier, R. Dendievel, A. Ayral, Mechanical properties of hierarchical porous silica thin films: Experimental characterization by nanoindentation and Finite Element modeling, *Microporous Mesoporous Mater.* 140 (2011) 120–129. doi:10.1016/j.micromeso.2010.09.004.
- [52] X. Chen, Y. Xiang, J.J. Vlassak, Novel technique for measuring the mechanical properties of porous materials by nanoindentation, *J. Mater. Res.* 21 (2006) 715–724. doi:10.1557/jmr.2006.0088.
- [53] A.A. Volinsky, J.B. Vella, W.W. Gerberich, Fracture toughness, adhesion and mechanical properties of low-K dielectric thin films measured by nanoindentation, *Thin Solid Films.* 429 (2003) 201–210. doi:10.1016/S0040-6090(03)00406-1.
- [54] G. Colas, A. Saulot, N. Bouscharain, C. Godeau, Y. Michel, Y. Berthier, How far does contamination help dry lubrication efficiency?, *Tribol. Int.* 65 (2013) 177–189. doi:10.1016/j.triboint.2012.12.011.
- [55] C.G. Sammis, M.F. Ashby, The failure of brittle porous solids under compressive stress states, *Acta Metall.* 34 (1986) 511–526. doi:10.1016/0001-6160(86)90087-8.
- [56] S. Samborski, T. Sadowski, Experimental Investigations and Modelling of Porous Ceramics, in: S. Samborski (Ed.), IUTAM Symp. Multiscale Model. Damage Fract.

- Process. Compos. Mater., Springer, 2006: pp. 263–270.
- [57] E. Gnecco, *Fundamentals of Friction and Wear*, Springer, 2007. doi:10.1007/978-3-540-36807-6.
- [58] A.A. Voevodin, J.S. Zabinski, C. Muratore, *Recent Advances in Hard , Tough , and Low Friction Nanocomposite Coatings New Directions in Hard Coatings*, Tsinghua Sci. Technol. 10 (2005) 665–679.
- [59] A.H. Chokshi, A. Rosen, J. Karch, H. Gleiter, On the validity of the Hall-Petch relationship in nanocrystalline materials, *Scr. Metall.* 23 (1989) 1679–1684. doi:10.1016/j.egypro.2009.02.265.
- [60] P. Stempflé, J. Von Stebut, Nano-mechanical behaviour of the 3rd body generated in dry friction - Feedback effect of the 3rd body and influence of the surrounding environment on the tribology of graphite, *Wear.* 260 (2006) 601–604. doi:10.1016/j.wear.2005.03.021.
- [61] K.J. Wahl, D.N. Dunn, I.L. Singer, Wear behavior of Pb-Mo-S solid lubricating coatings, *Wear.* 230 (1999) 175–183. doi:10.1016/S0043-1648(99)00100-3.
- [62] J.R. Lince, Tribology of co-sputtered nanocomposite Au/MoS<sub>2</sub> solid lubricant films over a wide contact stress range, *Tribol. Lett.* 17 (2004) 419–428. doi:10.1023/B:TRIL.0000044490.03462.6e.
- [63] F. Gustavsson, S. Jacobson, A. Cavaleiro, T. Polcar, Frictional behavior of self-adaptive nanostructural Mo-Se-C coatings in different sliding conditions, *Wear.* 303 (2013) 286–296. doi:10.1016/j.wear.2013.03.032.
- [64] A. a. Tedstone, D.J. Lewis, R. Hao, S.-M. Mao, P. Bellon, R.S. Averback, C.P. Warrens, K.R. West, P. Howard, S. Gaemers, S.J. Dillon, P. O'Brien, Mechanical Properties of Molybdenum Disulfide and the Effect of Doping: An in Situ TEM Study, *ACS Appl. Mater. Interfaces.* 7 (2015) 20829–20834. doi:10.1021/acsami.5b06055.
- [65] D.-M. Tang, D.G. Kvashnin, S. Najmaei, Y. Bando, K. Kimoto, P. Koskinen, P.M. Ajayan, B.I. Yakobson, P.B. Sorokin, J. Lou, D. Golberg, Nanomechanical cleavage of molybdenum disulphide atomic layers, *Nat. Commun.* 5 (2014) 922872–922872. doi:10.1038/ncomms4631.
- [66] E.E. Hoffman, L.D. Marks, Soft Interface Fracture Transfer in Nanoscale MoS<sub>2</sub>, *Tribol. Lett.* 64 (2016) 1–10. doi:10.1007/s11249-016-0743-2.